Spectro-temporal dispersion management of femtosecond pulses for fiber-optic two-photon endomicroscopy

WENXUAN LIANG,[1,2] GUNNSTEINN HALL,[1,2] AND XINGDE LI[1,*]

[1]*Department of Biomedical Engineering, Johns Hopkins University, 720 Rutland Ave, Baltimore, Maryland, 21205, USA*
[2]*These two authors contributed equally to this work*
*xingde@jhu.edu

Abstract: The emerging fiber-optic two-photon endomicroscopy technology holds a strong promise for enabling translational applications of nonlinear optical imaging. Effective femtosecond pulse dispersion management is critical for achieving high-quality imaging. Here we report systematic analyses and performance characterization of a dual-fiber spectro-temporal dispersion management scheme involving a grating pair as the pulse stretcher. Compared with conventional linear-only compensation, the grating-based spectro-temporal compensation also takes into account nonlinear effects and enhances the two-photon signal by ~3-fold as experimentally demonstrated. Numerical simulations were carried out to systematically investigate the influence of several key design parameters on the overall compensation efficacy. Furthermore, comprehensive performance comparison with an ideal grism-pair counterpart reveals that a grating-pair stretcher affords much higher power throughput and thus is preferable for portable endomicroscopy systems with limited laser source power.

References and links

1. F. Helmchen, M. S. Fee, D. W. Tank, and W. Denk, "A Miniature Head-Mounted Two-Photon Microscope. High-Resolution Brain Imaging in Freely Moving Animals," Neuron **31**(6), 903–912 (2001).
2. M. T. Myaing, D. J. MacDonald, and X. Li, "Fiber-optic scanning two-photon fluorescence endoscope," Opt. Lett. **31**(8), 1076–1078 (2006).
3. Y. Wu, Y. Leng, J. Xi, and X. Li, "Scanning all-fiber-optic endomicroscopy system for 3D nonlinear optical imaging of biological tissues," Opt. Express **17**(10), 7907–7915 (2009).
4. Y. Wu, J. Xi, M. J. Cobb, and X. Li, "Scanning fiber-optic nonlinear endomicroscopy with miniature aspherical compound lens and multimode fiber collector," Opt. Lett. **34**(7), 953–955 (2009).
5. S. Tang, W. Jung, D. McCormick, T. Xie, J. Su, Y.-C. Ahn, B. J. Tromberg, and Z. Chen, "Design and implementation of fiber-based multiphoton endoscopy with microelectromechanical systems scanning," J. Biomed. Opt. **14**(3), 034005 (2009).
6. Y. Zhao, H. Nakamura, and R. J. Gordon, "Development of a versatile two-photon endoscope for biological imaging," Biomed. Opt. Express **1**(4), 1159–1172 (2010).
7. D. R. Rivera, C. M. Brown, D. G. Ouzounov, I. Pavlova, D. Kobat, W. W. Webb, and C. Xu, "Compact and flexible raster scanning multiphoton endoscope capable of imaging unstained tissue," Proc. Natl. Acad. Sci. U.S.A. **108**(43), 17598–17603 (2011).
8. W. Liang, K. Murari, Y. Zhang, Y. Chen, M. J. Li, and X. Li, "Increased illumination uniformity and reduced photodamage offered by the Lissajous scanning in fiber-optic two-photon endomicroscopy," J. Biomed. Opt. **17**(2), 021108 (2012).
9. Y. Zhang, M. L. Akins, K. Murari, J. Xi, M.-J. Li, K. Luby-Phelps, M. Mahendroo, and X. Li, "A compact fiber-optic SHG scanning endomicroscope and its application to visualize cervical remodeling during pregnancy," Proc. Natl. Acad. Sci. U.S.A. **109**(32), 12878–12883 (2012).
10. G. Ducourthial, P. Leclerc, T. Mansuryan, M. Fabert, J. Brevier, R. Habert, F. Braud, R. Batrin, C. Vever-Bizet, G. Bourg-Heckly, L. Thiberville, A. Druilhe, A. Kudlinski, and F. Louradour, "Development of a real-time flexible multiphoton microendoscope for label-free imaging in a live animal," Sci. Rep. **5**(1), 18303 (2015).
11. W. Liang, G. Hall, B. Messerschmidt, M.-J. Li, and X. Li, "Nonlinear optical endomicroscopy for label-free functional histology *in vivo*," Light Sci. Appl. **6**(11), e17082 (2017).

12. W. R. Zipfel, R. M. Williams, and W. W. Webb, "Nonlinear magic: multiphoton microscopy in the biosciences," Nat. Biotechnol. **21**(11), 1369–1377 (2003).
13. G. P. Agrawal, *Nonlinear Fiber Optics,* 3rd ed. (Academic Press, San Diego, 2001).
14. E. Treacy, "Optical pulse compression with diffraction gratings," IEEE J. Quantum Electron. **5**(9), 454–458 (1969).
15. R. L. Fork, O. E. Martinez, and J. P. Gordon, "Negative dispersion using pairs of prisms," Opt. Lett. **9**(5), 150–152 (1984).
16. M. Oberthaler and R. A. Hopfel, "Special narrowing of ultrashort laser pulses by self-phase modulation in optical fibers," Appl. Phys. Lett. **63**(8), 1017–1019 (1993).
17. S. A. Planas, N. L. P. Mansur, C. H. B. Cruz, and H. L. Fragnito, "Spectral narrowing in the propagation of chirped pulses in single-mode fibers," Opt. Lett. **18**(9), 699–701 (1993).
18. A. Weiner, *Ultrafast Optics* (John Wiley & Sons, 2011).
19. S. W. Clark, F. Ö. Ilday, and F. W. Wise, "Fiber delivery of femtosecond pulses from a Ti:sapphire laser," Opt. Lett. **26**(17), 1320–1322 (2001).
20. P. L. François, "Nonlinear propagation of ultrashort pulses in optical fibers: total field formulation in the frequency domain," J. Opt. Soc. Am. B **8**(2), 276–293 (1991).
21. J. R. Dormand and P. J. Prince, "A family of embedded Runge-Kutta formulae," J. Comput. Appl. Math. **6**(1), 19–26 (1980).
22. L. F. Shampine and M. W. Reichelt, "The MATLAB ODE Suite," SIAM J. Sci. Comput. **18**(1), 1–22 (1997).
23. M. L. Akins, K. Luby-Phelps, and M. Mahendroo, "Second harmonic generation imaging as a potential tool for staging pregnancy and predicting preterm birth," J. Biomed. Opt. **15**(2), 026020 (2010).
24. M. Lelek, E. Suran, F. Louradour, A. Barthelemy, B. Viellerobe, and F. Lacombe, "Coherent femtosecond pulse shaping for the optimization of a non-linear micro-endoscope," Opt. Express **15**(16), 10154–10162 (2007).
25. E. A. Gibson, D. M. Gaudiosi, H. C. Kapteyn, R. Jimenez, S. Kane, R. Huff, C. Durfee, and J. Squier, "Efficient reflection grisms for pulse compression and dispersion compensation of femtosecond pulses," Opt. Lett. **31**(22), 3363–3365 (2006).
26. C. Lefort, T. Mansuryan, F. Louradour, and A. Barthelemy, "Pulse compression and fiber delivery of 45 fs Fourier transform limited pulses at 830 nm," Opt. Lett. **36**(2), 292–294 (2011).
27. M. Kalashyan, C. Lefort, L. Martínez-León, T. Mansuryan, L. Mouradian, and F. Louradour, "Ultrashort pulse fiber delivery with optimized dispersion control by reflection grisms at 800 nm," Opt. Express **20**(23), 25624–25635 (2012).
28. C. Lefort, M. Kalashyan, G. Ducourthial, T. Mansuryan, R. P. O'Connor, and F. Louradour, "Sub-30-fs pulse compression and pulse shaping at the output of a 2-m-long optical fiber in the near-infrared range," J. Opt. Soc. Am. B **31**(10), 2317–2324 (2014).
29. W. M. Lee and S. H. Yun, "Adaptive aberration correction of GRIN lenses for confocal endomicroscopy," Opt. Lett. **36**(23), 4608–4610 (2011).
30. C. Wang and N. Ji, "Characterization and improvement of three-dimensional imaging performance of GRIN-lens-based two-photon fluorescence endomicroscopes with adaptive optics," Opt. Express **21**(22), 27142–27154 (2013).
31. R. P. Barretto, B. Messerschmidt, and M. J. Schnitzer, "In vivo fluorescence imaging with high-resolution microlenses," Nat. Methods **6**(7), 511–512 (2009).
32. J. Xi, A. Zhang, Z. Liu, W. Liang, L. Y. Lin, S. Yu, and X. Li, "Diffractive catheter for ultrahigh-resolution spectral-domain volumetric OCT imaging," Opt. Lett. **39**(7), 2016–2019 (2014).
33. G. Matz, B. Messerschmidt, and H. Gross, "Design and evaluation of new color-corrected rigid endomicroscopic high NA GRIN-objectives with a sub-micron resolution and large field of view," Opt. Express **24**(10), 10987–11001 (2016).
34. M. Tsang, D. Psaltis, and F. G. Omenetto, "Reverse propagation of femtosecond pulses in optical fibers," Opt. Lett. **28**(20), 1873–1875 (2003).
35. M. Pawłowska, A. Patas, G. Achazi, and A. Lindinger, "Parametrically shaped femtosecond pulses in the nonlinear regime obtained by reverse propagation in an optical fiber," Opt. Lett. **37**(13), 2709–2711 (2012).
36. A. Chong, J. Buckley, W. Renninger, and F. Wise, "All-normal-dispersion femtosecond fiber laser," Opt. Express **14**(21), 10095–10100 (2006).
37. W. Fu, L. G. Wright, P. Sidorenko, S. Backus, and F. W. Wise, "Several new directions for ultrafast fiber lasers [Invited]," Opt. Express **26**(8), 9432–9463 (2018).

1. Introduction

The emerging two-photon endomicroscopy technology is critical for translational clinical applications of nonlinear microscopy, and recent studies have demonstrated its strong promise to enable functional histological imaging of internal organs *in vivo*, *in situ* and in real time [1–10]. To develop an endomicroscope that truly lends itself to practical label-free imaging applications, the imaging signal-to-noise ratio (SNR) is of paramount importance [11]. Since two-photon excitation (2PE) efficiency scales reciprocally with the temporal pulsewidth [12], effective dispersion management is indispensable to fiber delivery of ultrafast laser pulses to

the distal end of the endomicroscope. It is well-known that a femtosecond laser pulse, when propagating through an optical fiber, is subject to temporal broadening induced by both linear dispersion and nonlinear effects [13]. The principal linear dispersion, the group delay dispersion (GDD), can be compensated by giving the shorter-wavelength component (which propagates slower in fiber) an appropriate head start; such negative pre-chirping can be realized by several methods such as a grating pair- or a prism sequence-based pulse shaper [14,15]. In the femtosecond regime, however, such a linear compensation method is only effective for very low-energy pulses. Even at a sub-ten mW average power, the peak intensity of a 150-fs pulse (e.g., at 800 nm with an 80 MHz repetition rate) launched into a single-mode fiber core (~5 μm in diameter) is high enough to induce substantial nonlinear effects and spectral changes, thus making linear-only dispersion compensation ineffective. Indeed, previous research has shown that the primary nonlinear effect, named self-phase modulation (SPM), can suppress the spectral bandwidth of a negatively-chirped ultrashort laser pulse [16,17]. Therefore, the negative pre-chirping GDD-compensation method always ends up with a narrowed spectral bandwidth, and temporal broadening is essentially inevitable as prescribed by the universal lower bound of time-bandwidth product [18]. This also explains previous observations that, starting with transform-limited 150 fs pulses, the best achievable pulsewidth out of an endomicroscope of an ~70 cm fiber length was on the order of ~400-500 fs FWHM [1,7,9].

Since negative pre-chirping is indispensable to balance the positive in-fiber GDD within the typical 2PE wavelength range (700-1000 nm), an intuitive idea to counteract such inevitable SPM-induced spectral narrowing is to start with a pulse of broader spectral bandwidth. One easy-to-implement solution is to couple the initial unchirped pulses first into a piece of single-mode fiber (SMF), in which the SPM effect functions to broaden (rather than compress) the pulse spectrum [13]. Spectrally broadened pulses out of the first SMF are then negatively chirped and launched into the single-mode core of a second fiber (often a double-clad fiber (DCF) in the two-photon endomicroscope), which restores both the spectral bandwidth and the temporal pulsewidth while delivering the pulses to the distal end of the endomicroscope [19]. In this manuscript, we will present detailed performance characterization and operational optimization of such dual-fiber spectro-temporal dispersion compensation scheme utilizing a grating pair as the pulse stretcher. Besides experimentally quantifying the enhancement of the two-photon signal, we undertook comprehensive numerical simulations which reveal practical guidelines for optimized operation of the grating pair-based spectro-temporal dispersion compensation scheme. Furthermore, we theoretically (by simulation) compared the grating pair with an ideal grism pair under different practical contexts, which elucidates the respective merits of each method.

2. Methods

2.1 Experimental setup

The setup for characterizing our grating pair-based dual-fiber femtosecond pulse delivery scheme is shown in Fig. 1, which is under the operational context of our recently developed fiber-optic two-photon endomicroscopy system [11]. Briefly, transform-limited near infrared (NIR) laser pulses out of a Ti:Sapphire laser (Chameleon Vision II, Coherent Inc., California), ~150 fs FWHM with an 80 MHz repetition rate, are launched into a piece of ~30-cm-long polarization-maintaining single-mode fiber (PM-SMF; PM780-HP, Thorlabs, New Jersey). Using a PM-SMF ensures that the output light stays nearly linearly polarized with polarization direction perpendicular to grating grooves for better diffraction efficiency. The pulse spectrum becomes broadened due to the interaction between positive chirping and SPM effect in the PM-SMF (dash box labeled as Spectral Broadening (SB) in Fig. 1). Pulses out of the PM-SMF are first collimated via a customized achromatic triplet, then pass through a pair of volume holographic transmission gratings (600 lpmm; Wasatch Photonics, North Carolina) to gain sufficient negative pre-chirping, and finally are coupled into the core of the DCF (~0.8

meter long), in which the spectrum gets recompressed due to the SPM effect while the survived spectral components get re-aligned in phase to recover a short temporal pulsewidth when exiting the endomicroscope. For a single-fiber linear-only compensation scheme, the SB module in Fig. 1 was bypassed using flip-mirrors with the grating separation retuned accordingly to provide an appropriate amount of anomalous GDD. To measure the pulsewidth, light emanating from the endomicroscope was collimated and guided to a home-built SHG intensity autocorrelator [18], while pulse spectra at different locations of the endomicroscopy system (e.g., out of the Ti:Sapphire laser, output from the SMF, and output from the DCF) were measured by directing the light, after being appropriately attenuated, to a miniature spectrometer (BLUE-wave, StellarNet, Florida).
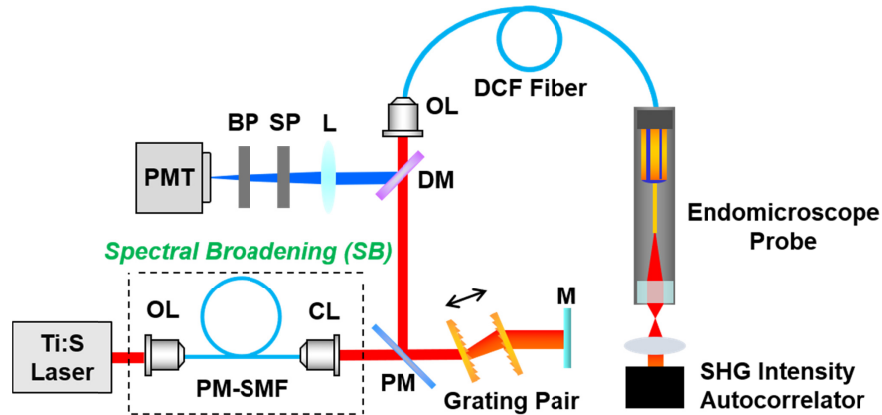

Fig. 1. System schematic and experimental configurations. The spectral broadening (SB) module is bypassed for single-fiber linear-only dispersion compensation. BP: band-pass filter; CL: collimating lens; DM: dichroic mirror; L: collection lens; M: mirror; OL: objective lens; PM: pick-up mirror; PMT: photomultiplier; SP: short-pass optical filter.

Detailed working principles of the two-photon endomicroscopy system have been described elsewhere [2,8,11]. Briefly, the excitation light delivered to the distal end of the endomicroscope is focused into the specimen using an achromatic micro-objective lens with an effective NA of ~0.5 and resulted resolution of ~0.7 μm × 6.5 μm (lateral × axial). The emission photons (fluorescence or SHG) are epi-collected mainly into the inner clad of the DCF, guided back to the proximal end, and then separated from the excitation beam via a dichroic filter (FF665-Di02-25x36, Semrock). A short-pass optical filter (FF01-680/SP-25, Semrock) is deployed in front of the photomultiplier (PMT, H10771P-40, Hamamatsu) to further eliminate the residual excitation light. For SHG imaging at the 890 nm central wavelength, an additional 445/20 nm band-pass optical filter (FF01-445/20-25, Semrock) is used to separate the SHG detection band.

2.2 Optimization of grating separation

It is known that optimal pulsewidth appears when the anomalous GDD provided by the grating pair or grism pair roughly balances the total normal GDD of both fibers [19], as we have also observed both in experiments and in numerical simulation. In practice, once the grating separation is set near the target optimal value, one needs to fine-tune the separation with an objective and sensitive criterion. One criterion is to measure and minimize the FWHM of the intensity ACF of the output pulse using the autocorrelator described above; however, since the shape and FWHM of the intensity ACF is insensitive to subtle changes in pulse profile outside the main lobe (e.g. trailing or leading tails due to TOD), this procedure can be error-prone. We found out in practice that a more robust approach is to directly maximize the final 2PE efficiency. One way to do this is submerging the endomicroscope in a

home-made 2-μM solution of fluorescein (Sigma-Aldrich), and counting the emission rate of epi-collected 2PF photons using a time-correlated single-photon counting module (SPC 150, Becker & Hickl GmbH). Note that such submersion configuration makes sure the collection efficiency stays the same across multiple experiments. Therefore, we can fairly compare the 2PE efficiency between the single-fiber linear-only configuration and the dual-fiber spectro-temporal dispersion compensation configurations.

2.3 Pulse propagation simulation

Simulations were carried out to investigate the evolution of the pulse profile through the endomicroscopy system. The simulation procedure for the dual-fiber spectro-temporal dispersion compensation scheme starts with a transform-limited femtosecond pulse. The pulse propagates first through the PM-SMF (i.e. the first fiber), then a grating- or grism-based pulse stretcher, and finally the single-mode core of the DCF (i.e. the second fiber). We adopted the total field formulation in the frequency domain to simulate the nonlinear pulse propagation in optical fibers [20]. The basic concepts and key parameters that are necessary for understanding the simulation results are detailed below.

2.3.1 Frequency-domain E-field propagation in optical fibers

Following the total field formulation [20], the electric field of an ultrafast pulse can be represented as

$$\boldsymbol{E}(z,t,r) \propto \psi(r) \, Re\left\{ A(z,\tau) e^{j\left[\omega_0 t - \beta(\omega_0)z\right]} \right\}, \tag{1}$$

where $A(z,\tau)$ denotes the dimensionless amplitude function, $\psi(r)$ the radially symmetric E-field distribution, $\beta(\omega)$ the mode-propagation constant in fiber, and $\tau = t - z / V_0 = t - z\beta_0^{(1)}$ the retarded (local) time with V_0 denoting the group velocity of the pulse at a carrier frequency ω_0, i.e. $V_0^{-1} = \partial_\omega \beta(\omega_0)$. For simplicity, in our simulations the mode-propagation constant $\beta(\omega)$ is approximated by the material dispersion of fused silica as $\beta(\omega) = 2\pi n(\omega) / \lambda$ with the refractive index $n(\omega)$ given by the well-known Sellmeier equation.

Taking the weakly guiding approximation $n_{\mathrm{core}} \approx n_{\mathrm{clad}} \doteq n_0$, the instantaneous total power of an ultrashort pulse at any given distance z and local time τ, integrated across the entire beam profile, is equal to

$$P(z,\tau) = \iint \frac{n_0}{2\mu_0 c} \left| \boldsymbol{E}(z,t,r) \right|^2 \mathrm{d}x\mathrm{d}y \doteq P_{\mathrm{scale}} \cdot \left| A(z,\tau) \right|^2. \tag{2}$$

Here μ_0 and c denote the linear permeability and the speed of light in vacuum, respectively, and P_{scale} represents the power scale which absorbs all time-independent factors in the equation. Basically P_{scale} scales with the pulse energy (or equivalently the average light power) [20]. The strength of in-fiber nonlinear effects is related to P_{scale} (i.e., the laser power), $A(z,\tau)$ (i.e., the temporal pulse shape), and $\psi(r)$ (i.e., the spatial mode distribution). In simulation, P_{scale} can be determined from the pulse energy and the initial pulse profile, while the pulse energy equals average laser power divided by the pulse repetition rate. Especially, assuming a sech²-shaped intensity profile and thus an initial amplitude function $A(0,\tau) = \mathrm{sech}(\tau / \tau_0)$, we can evaluate the pulse energy by

$$E_{\text{pulse}} = P_{\text{scale}} \cdot \int \text{sech}^2 \left(\tau / \tau_0 \right) d\tau = 2\tau_0 \cdot P_{\text{scale}}. \tag{3}$$

And the FWHM temporal pulsewidth is $\tau_{FWHM} = 2\ln\left(\sqrt{2}+1\right)\tau_0$. Since $\max|A(0,\tau)| = 1$, the power scale P_{scale} here corresponds also to the peak instantaneous power of the initial pulse. Therefore, the nonlinear length can be calculated as

$$L_{\text{NL}} = \frac{\lambda A_{\text{eff}}}{2\pi n_2^I P_{\text{scale}}} = \frac{\lambda \cdot \text{MFD}^2}{8 n_2^I \cdot P_{\text{scale}}}. \tag{4}$$

where A_{eff} is the effective core area and is approximated by $\pi \cdot \text{MFD}^2 / 4$ above (where MFD is short for mode-field diameter) and n_2^I denotes the nonlinear-index coefficient [13]. For the 890-nm wavelength used in this manuscript, the value of n_2^I is taken as 2.7×10^{-20} m²/W [13]. In our simulations, the time constant τ_0 is set to 85.09 fs so that the initial FWHM pulsewidth equals 150 fs, and the mode-field diameter is set to 5.0 μm for both the SMF and the DCF.

Defining the temporal Fourier transform of $A(z,\tau)$ as $\tilde{A}(z,\Omega) = \int A(z,\tau) e^{-j\Omega\tau} d\tau$, pulse propagation in the frequency domain is carried out following the propagation equation in Ref [20] (which is equivalent to the nonlinear Schrödinger equation in the time domain [13]). For simplicity, the in-fiber attenuation has been ignored since the propagation distance considered here is only on the order of meters. In this way, the temporal integral of the squared modulus of E-field amplitude $\int |A(z,\tau)|^2 d\tau$ stays constant over propagation [20], and thus the average light power propagating in the SMF or DCF is controlled purely by P_{scale} in our simulation. The frequency-domain propagation equation is solved by the Runge-Kutta method using the built-in ordinary differential equation (ODE) solver *ode45* in MATLAB (MATLAB R2016b, Mathworks, Natick, MA) [21,22]. Numerically, the amplitude function is digitized into 8192 discrete time points (also the FFT length) with 2-fs sampling interval, thereby covering a temporal range of 16.384 ps and a frequency bandwidth of 500 THz, both wide enough for ranges encountered in the simulation.

2.3.2 Negative chirping from the grating- and grism-pair stretcher

Numerically, both the grating-pair and the grism-pair stretchers are implemented by adding extra spectrally dependent phase in the frequency domain of the pulse amplitude function, and the practical power throughput (or loss) is simulated by reducing the total pulse energy, i.e., by decreasing the power scale parameter P_{scale}. With details about $P_{\text{SMF}} / P_{\text{DCF}}$ ratio (always larger than one) provided in the main text, described here are phase functions of grating- and grism-pair pulse stretchers employed in our simulation.

Given a grating pair, denoting the groove period by *d*, the grating separation (along the grating surface normal direction) by *G*, and the incident and diffraction angles by θ_i and θ_d, respectively, the total double-pass phase delay is [14]

$$\Psi(\omega) = 2\omega(\Lambda + G\cos\theta_d)/c, \tag{5}$$

where Λ denotes the common in-air propagation distance shared by all wavelengths. Starting from this, the double-pass GDD and TOD furnished by the grating pair can be found from $\partial^2\Psi / \partial\omega^2$ and $\partial^3\Psi / \partial\omega^3$, respectively. Explicitly, we have:

$$\text{GDD}(\omega) = \frac{\partial^2\Psi}{\partial\omega^2} = -\frac{8\pi^2 cG}{\omega^3 d^2 \cos^3\theta_d}. \tag{6}$$

And the TOD can be calculated further as

$$\text{TOD}(\omega) = \frac{\partial^3 \Psi}{\partial \omega^3} = -\frac{3}{\omega}\left(1 + \frac{\lambda}{d}\cdot\frac{\sin\theta_d}{\cos^2\theta_d}\right)\cdot\frac{\partial^2\Psi}{\partial\omega^2}. \tag{7}$$

As manifested in the two equations above, the TOD and GDD provided by a grating pair are of opposite sign.

The dispersion provided by a grating pair is implemented directly in frequency domain via [20]

$$\tilde{A}_{\text{grating}}(\text{out}, \Omega) = \tilde{A}(\text{in}, \Omega)\cdot e^{-j\cdot\left[\Psi(\omega_0+\Omega)] - \Psi(\omega_0) - \frac{\partial\Psi(\omega_0)}{\partial\omega}\cdot\Omega\right]}$$

$$\approx \tilde{A}(\text{in}, \Omega)\cdot e^{-j\cdot\left[\frac{\partial^2\Psi(\omega_0)}{\partial\omega^2}\cdot\frac{\Omega^2}{2} + \frac{\partial^3\Psi(\omega_0)}{\partial\omega^3}\cdot\frac{\Omega^3}{6}\right]}. \tag{8}$$

The first line in Eq. (8) takes into account all higher-order phases, while the second line accounts for only the GDD and TOD terms. We numerically compared the two methods and found that they give almost identical outputs for the fiber length range of interest here; we adopted the second line in our simulation to be consistent with the grism phase function as described below.

To investigate all setup parameters featured by a practical grism pair is beyond the scope of this study, and thus in our simulation without loss of generality, we assume an *ideal grism pair* which provides anomalous GDD and TOD that cancel exactly the GDD and TOD induced by optical fibers. Therefore, the grism-pair phase function can be simply calculated as

$$\tilde{A}_{\text{grism}}(\text{out}, \Omega) = \tilde{A}(\text{in}, \Omega)\cdot e^{-j\cdot\left[\beta_0^{(2)}\cdot\frac{\Omega^2}{2} + \beta_0^{(3)}\cdot\frac{\Omega^3}{6}\right]\cdot L_{\text{total}}}, \tag{9}$$

where L_{total} is the total length of SMF and DCF, and $\beta_0^{(k)} \doteq \dfrac{\partial^k\beta(\omega_0)}{\partial\omega^k}$ the chromatic dispersion of optical fiber at the central frequency ω_0. Such an ideal grism-pair stretcher basically cancels out both GDD and TOD of the two fibers.

2.3.3 Evaluation of 2PE efficiency

Both temporal pulsewidth and spectral bandwidth can be evaluated from the final amplitude function $A(z,\tau)$ out of the second fiber (i.e. the DCF). The root-mean-square (rms) pulsewidth and bandwidth are adopted in this manuscript to characterize the overall temporal intensity profile or spectral power density distribution [18]:

$$\Delta\tau_{\text{rms}}(z) = 2\cdot\sqrt{\frac{\int\tau^2|A(z,\tau)|^2\,d\tau}{\int|A(z,\tau)|^2\,d\tau} - \left(\frac{\int\tau|A(z,\tau)|^2\,d\tau}{\int|A(z,\tau)|^2\,d\tau}\right)^2}, \tag{10}$$

$$\Delta\nu_{\text{rms}}(z) = \frac{1}{\pi}\cdot\sqrt{\frac{\int\Omega^2|\tilde{A}(z,\Omega)|^2\,d\Omega}{\int|\tilde{A}(z,\Omega)|^2\,d\Omega} - \left(\frac{\int\Omega|\tilde{A}(z,\Omega)|^2\,d\Omega}{\int|\tilde{A}(z,\Omega)|^2\,d\Omega}\right)^2}. \tag{11}$$

The resultant absolute two-photon signal strength is basically proportional to the integral of instantaneous pulse power squared, i.e.

$$I_{\text{2PF}} \propto \int P^2(z,\tau)\,d\tau = P_{\text{scale}}^2\cdot\int|A(\text{DCF output},\tau)|^4\,d\tau. \tag{12}$$

Furthermore, to compare the temporal profiles (shapes) of pulses of different powers, we are interested in a power-independent quantification of how well the pulse profile lends itself to efficient 2PE. This can be simply evaluated via

$$\frac{I_{2\text{PF}}}{P_{\text{scale}}^2} = \int \left| A(\text{DCF output}, \tau) \right|^4 d\tau. \tag{13}$$

Since the integral $\int \left| A(z, \tau) \right|^2 d\tau$ stays invariant through propagation, this *normalized 2PE efficiency* as defined above favors basically a short pulsewidth, and will be adopted as a universal, power-independent criterion of the efficacy of dispersion compensation in this manuscript.
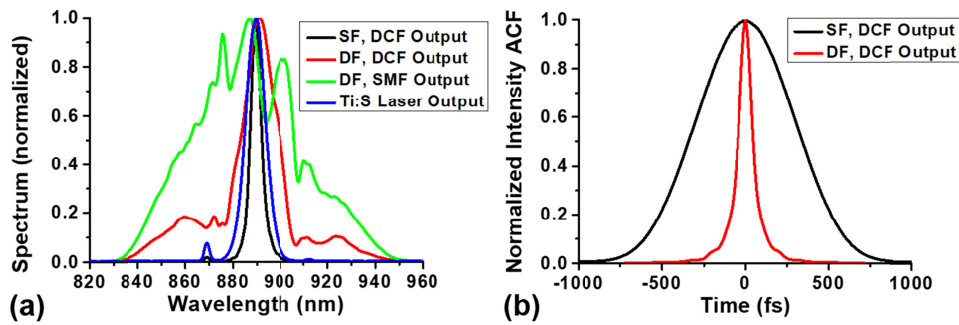
3. Experimental characterization

Fig. 2. Characterization of dual-fiber spectro-temporal dispersion compensation. (a) Evolution of pulse spectra through the entire system for both single-fiber (SF) linear-only and dual-fiber (DF) spectro-temporal dispersion compensation schemes. The curves were measured at an 890-nm central wavelength with an ~180 mW average power in the SMF and an ~48 mW power in the DCF. SPM-induced spectral narrowing of negatively-chirped pulses is manifest both in single-fiber scheme by comparing the DCF output spectrum (black curve) to the Ti:Sapphire laser spectrum (blue curve), and in dual-fiber scheme by comparing the DCF output spectrum (red curve) to the SMF output spectrum (green). (b) Intensity auto-correlation function of laser pulses out of the DCF with different dispersion compensation schemes. The FWHM of the two ACFs are ~660 fs and ~100 fs, respectively.

3.1 Characterization of spectral bandwidth and temporal pulsewidth

An example of evolving pulse spectrum is illustrated in Fig. 2a. Compared with the spectrum of the original transform-limited pulse exiting the laser, the spectral broadening in the PM-SMF (green curve in Fig. 2a) and re-compression in the DCF (red curve in Fig. 2a) are evident. One would notice that the final output spectrum is still much broader than the original laser spectrum (blue curve in Fig. 2a), i.e., the spectrum is not fully restored. This is attributed to the lower average power and thus relatively weaker SPM effect in the DCF than those in the SMF. Such a broadened spectrum supports an even narrower temporal pulsewidth out of the DCF, as reflected in the intensity autocorrelation function (ACF) measurement (red curve in Fig. 2b). For comparison, under the circumstance of linear-only dispersion, i.e., bypassing the SMF in Fig. 1, the optimal pulsewidth obtained at the same output power level is associated with a narrowed spectrum (FWHM of ~4.8 nm, black curve in Fig. 2a) and a much broadened temporal pulsewidth with an intensity ACF FWHM of ~660 fs (black curve in Fig. 2b).

Compared with the single-fiber linear-only counterpart, the FWHM of the intensity ACF yielded by the spectro-temporal dispersion compensation scheme (i.e., the dual-fiber approach) is narrowed by ~6.6-fold (i.e., from ~660 fs to ~100 fs). While the temporal pulsewidth reduction observed in intensity ACF measurements doesn't translate to the same

extent of two-photon signal enhancement, as discussed shortly, the results still demonstrate clearly the significant advantage in effective pulse delivery enabled by the spectro-temporal dispersion compensation scheme.

3.2 Quantification of 2PE improvement

To experimentally quantify the enhancement in 2PE efficiency, we undertook 2PF intensity measurement of a uniform fluorescein solution (10 μM) and SHG imaging of an *ex vivo* mouse cervical tissue section, using the single- and dual-fiber compensation methods with identical incident power and their respective optimal grating separations (both optimized for an output power of ~48 mW exiting from the DCF at 890 nm).
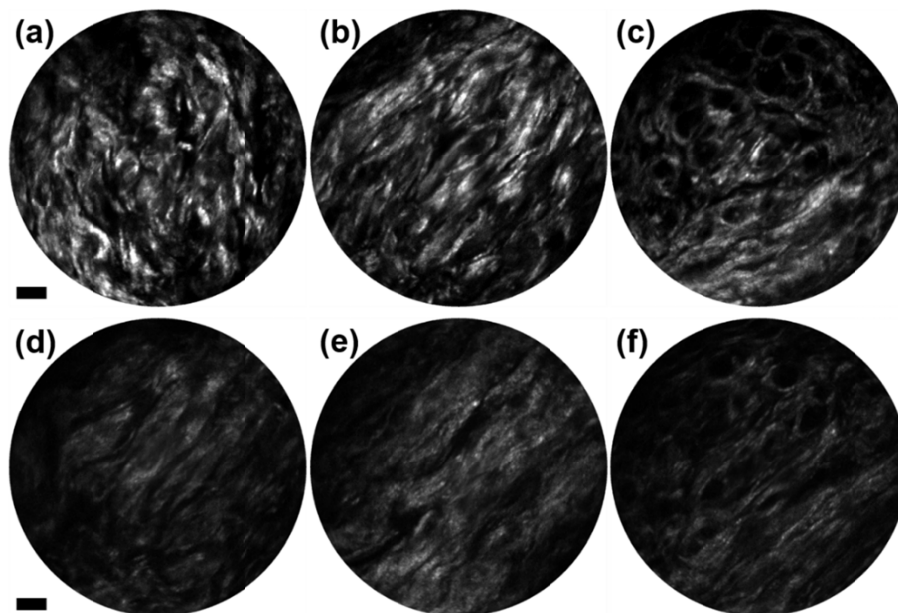

Fig. 3. SHG imaging-based comparison between single- and dual-fiber compensation schemes. Juxtaposed here for comparison are SHG images of an *ex vivo* mouse cervical tissue section acquired with dual-fiber spectro-temporal (a-c) and single-fiber linear-only (d-f) dispersion compensation schemes, respectively, both with ~40 mW incident power at 890 nm center wavelength on the sample. Scale bars: 10 μm.

For 2PF intensity measurement, by submerging the endomicroscope tip into the fluorescein solution, we ensure that the collection efficiency stays the same between experiments. Results showed that the dual-fiber configuration enhanced the 2PF signal by ~2.6- to ~3.2-fold, with a DCF output power ranging from ~16 to ~40 mW. The signal enhancement is more profound at a higher DCF power, which is expected since for the single-fiber linear-only dispersion compensation scheme both spectral suppression and temporal broadening are more dramatic at higher propagation power.

In addition to 2PF imaging of fluorescein solution, SHG imaging of *ex vivo* cervical tissue sections (50 μm thick) was also performed to evaluate the enhancement of the 2PE efficiency with the dual-fiber spectro-temporal dispersion management scheme. Regarding tissue sample preparation, briefly, the entire cervix was harvested from a pregnant mouse sacrificed at gestation day 18, snap-frozen in liquid nitrogen temperature, and then cut into 50-μm-thick sections and mounted onto microscope slides [9,23]. Such prepared tissue section was then thawed in room temperature and immersed in phosphate buffered saline (PBS) for imaging. The same tissue section was imaged by the same endomicroscope under the same incident power but under two compensation schemes (i.e., the single-fiber linear-only and the dual-

fiber spectro-temporal dispersion compensation schemes). To avoid the influence of the spatial variation of collagen fibers on the collected SHG signals, images were obtained from multiple quasi-randomly selected locations at the same depth (controlled by a 3D manipulator) under each compensation configuration. Representative SHG images are shown in Fig. 3, where the increase of the signal intensity and the signal-to-noise ratio under the dual-fiber compensation scheme is remarkable. Quantitatively, by averaging over many fields of view (FOVs), we estimate that the spectro-temporal compensation promotes the SHG signal strength by ~2.7-fold on average.

One immediately notices that the extent of experimentally measured two-photon signal enhancement (~2.7× to 3.2×) falls below the ~6.6-fold temporal pulsewidth reduction as derived from the intensity ACF. This discrepancy results mainly from the difference in the detailed pulse shapes between the two cases since the grating pair compensates only the GDD and leaves higher-order dispersions (mainly TOD) unbalanced. In fact, the TOD induced by the grating pair cumulates with the fiber TOD and results in increased trailing tails in the final pulse profile, which disperses pulse energy and compromises the overall 2PE efficiency [13,20,24].

4. Theoretical analyses by simulation

To understand the impact from higher-order dispersion, particularly the TOD, on the final pulsewidth and 2PE efficiency in our current grating pair-based endomicroscopy system, and to seek for practical guidance, we undertook numerical simulations to investigate the evolution of the pulse profile through the dual-fiber dispersion management procedure.

Details of the simulation are explained in Section 2.3. Since the kernel component of interest here is the pulse stretcher, careful characterization of operational parameters (e.g., incident angle and throughput) of the grating pair is critical for simulation accuracy. The volume holographic grating (VHG) employed in our endomicroscopy system can afford a single-pass efficiency up to 90% at the design wavelength (890 nm), yielding a four-pass overall power throughput of more than 60%. Even off the peak diffraction wavelength (e.g., at 750 nm), the overall 4-pass power throughput of the grating pair can still achieve ~30% under the Littrow configuration. Considering a typical single-mode fiber coupling efficiency of ~80% at around 800 nm, the power launched into the DCF core (after the grating pair) is about 50% (i.e., ~60% × 80%) to 25% (i.e., ~30% × 80%) of the power launched into (propagating within) the PM-SMF (i.e., the first fiber); therefore, in our simulation study, the SMF-to-DCF power ratio is set to either 2 or 4 for a grating-based stretcher. Furthermore, two different groove densities, 600 lpmm and 900 lpmm, are compared since the TOD/GDD ratio of a grating pair is density-dependent. Without losing generality, the DCF length within the endomicroscope is fixed at 1.0 m for all simulations.

4.1 Dependence on SMF length and in-fiber power

The group velocity dispersion (GVD) inside a fiber is ~29.2 fs^2/mm at 890 nm (as approximated by the material GVD of fused silica). For an initial sech^2 pulse ~150 fs in FWHM pulsewidth, the dispersion length is calculated to be $L_D = \tau_{FWHM}^2 / GVD = 77.1$ cm [13]. For average input power $P_{SMF} = 30$ mW (80 MHz repetition rate), the peak instantaneous power of the initial pulse can be estimated to be ~2.21 kW; then the nonlinear length can be calculated according to Eq. (4) as $L_{NL} = 4.7$ cm. Since L_{NL} scales reciprocally with the initial pulse's peak power, it is even shorter for higher P_{SMF}; therefore, the nonlinear lengths for all P_{SMF}'s considered here are much shorter than the dispersion length. For SMF lengths less than L_D, pulse propagation is dominated by nonlinear SPM effect; while for longer SMFs, pulse evolution is governed by the interplay of both dispersion and nonlinearity.

Fundamentally, when an unchirped pulse enters the core of an SMF, the nonlinear SPM effect it experiences is strongest in the beginning portion (when the propagation distance is

comparable to the nonlinear length L_{NL}), and then subsides gradually along with propagation since the peak power (and peak intensity) subsides and the temporal pulsewidth grows continuously. Therefore, on one hand, a higher propagation power (thus a stronger nonlinear effect) and a longer SMF (thus a longer interaction distance) lead to a broader out-of-SMF pulse spectrum, which is beneficial for generating a shorter out-of-DCF pulsewidth later. On the other hand, since the rate of spectral broadening slows down gradually with propagation (and finally stops when the pulse stretches too long) while the total TOD accumulates (especially for propagation distances longer than the dispersion length L_D), there exists some optimal propagation distance beyond which the detrimental impact of the growing TOD on the final temporal pulse profile will outrun the marginal benefit from spectral broadening. In light of this, in practice one needs to prudently decide the SMF length in order to achieve an optimal balance between spectral broadening and cumulating TOD. It is expected that the best SMF length to pair with a grating-pair pulse stretcher will dependent on the propagation powers in both the SMF and DCF.
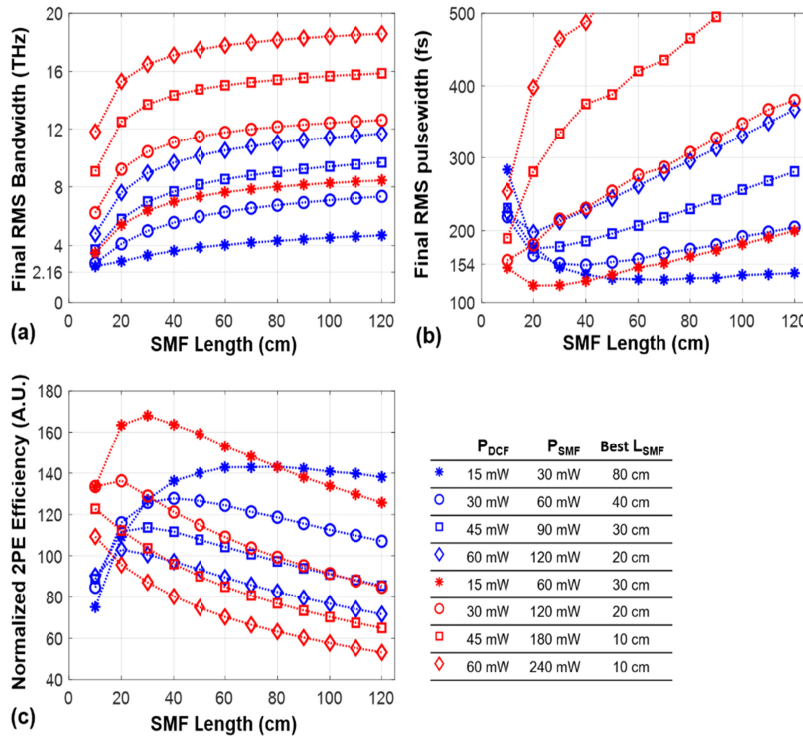

Fig. 4. Dependence of dispersion compensation efficacy on key operational parameters (i.e., the SMF length and laser power) of the grating pair-based spectro-temporal dispersion management scheme. The evolution of final rms bandwidth (a), rms pulsewidth (b), and normalized 2PE efficiency (c) with varying SMF length are compared at different power configurations. Different DCF powers are indicated by different types of markers, while the SMF-to-DCF power ratio is color-coded. The rms bandwidth and rms pulsewidth for the initial transform-limited pulse (890-nm center wavelength, 80 MHz repetition rate), ~2.16 THz and ~154 fs, are indicated in subfigure (a) and (b) respectively. The best SMF length (see the main text for definition) for each power configuration is provided in the legend. The grating groove density used for the simulation is 600 lpmm.

The theoretical analysis above is well supported by our simulation data. Plotted in Fig. 4 are the dependence of final root-mean-square (rms) pulsewidth (as defined in Eq. (10)), rms bandwidth (as defined in Eq. (11)), and normalized 2PE efficiency (as defined in Eq. (13)) out

of the DCF on various SMF lengths (ranging from 10 cm to 120 cm) and power configurations (with P_{DCF} ranging from 15 mW to 60 mW and P_{SMF}/P_{DCF} = 2 or 4). Based on these curves, several observations and comments are made in the following:

Firstly, as evident in Fig. 4(a), the final spectral bandwidth of pulses out of the DCF generally increases with longer SMF (for given P_{SMF} and P_{DCF} configuration) and higher P_{SMF} (for given SMF length and P_{SMF}/P_{DCF} ratio). It is noteworthy that spectral recompression in DCF never manages to restore the bandwidth back to the initial value of 2.16 THz, due to significantly lowered power level and therefore weakened nonlinear effects in the DCF. Although a broader bandwidth can ideally support a shorter pulsewidth, the final pulsewidth plotted in Fig. 4b doesn't simply match with the reciprocal of bandwidth shown in Fig. 4a; instead, it exhibits complicated dependence on the P_{SMF}/P_{DCF} ratio and the SMF length, implying the important role played by the uncompensated TOD and the resultant pulse distortion (e.g. trailing tails). Compared with the common FWHM pulsewidth, the rms pulsewidth can better characterize the temporal distribution of pulse energy. Especially, for each given P_{SMF} and P_{DCF} and P_{DCF} configuration, the evolution of rms pulsewidth in Fig. 4b matches well with the reciprocal of the corresponding normalized 2PE efficiency in Fig. 4c.

Secondly, for each power configuration (i.e., each curve in Fig. 4a-4c), there exists a best SMF length that leads to the highest normalized 2PE efficiency (equivalent to the best dispersion compensation efficacy). With all best SMF lengths tabulated in the legend of Fig. 4, we notice that the best SMF length decreases quickly with an increasing P_{SMF}, from 80 cm for P_{SMF} = 30 mW, to 30 cm for P_{SMF} = 60 mW, 20 cm for P_{SMF} = 120 mW, and finally to 10 cm for P_{SMF} = 180 mW and beyond (probably limited by the discrete set of SMF lengths simulated here). Furthermore, for each power configuration, the final normalized 2PE efficiency decays monotonically when the L_{SMF} goes beyond the respective best SMF length. These observations match well with our analysis on balancing between spectral bandwidth and total TOD. Specifically, for the cases of lower P_{SMF} and subsequently weaker SPM effect (i.e., the asterisk- or circle-marker blue curves in Fig. 4a-4c), the pulse spectrum grows slowly; therefore, a longer propagation in SMF could potentially help broaden the pulse spectrum. For the cases of higher P_{SMF} and subsequently stronger SPM effect (i.e., the square- or diamond-marker red curves in Fig. 4a-4c), the pulse spectrum broadens so rapidly with propagation that the detrimental effect of accumulating TOD quickly outruns the gain from a broader pulse spectrum and therefore a shorter SMF works out better.

Thirdly, we notice that for the cases of relatively higher P_{DCF} (i.e., the square- or diamond-marker curves in Fig. 4a-4c), a lower P_{SMF}/P_{DCF} ratio is generally advantageous, since the 2PE efficiency represented by the blue-colored curves in this groups are generally better than the red-colored counterparts. For the cases of relatively lower P_{DCF} (i.e., the asterisk- or circle-marker curves in Fig. 4c), however, a higher P_{SMF}/P_{DCF} ratio (corresponding to the red-colored curves) turns out better as long as the SMF length is maintained below 30 cm. Such distinct preference of P_{SMF}/P_{DCF} ratio stems again from the need for good trade-off between TOD and broadening pulse spectrum. Essentially, pulses of broader spectra are more vulnerable to higher order dispersions (e.g., TOD). Therefore, for a given P_{DCF} and an SMF length (thus a given TOD), the power in SMF should not be too high; otherwise, the benefit gained from broader pulse spectra can be overturned by the increased sensitivity to TOD.

Observations similar to what were discussed above were also found in simulation studies at the 750-nm center wavelength (data not shown for brevity). In summary, since a grating-pair pulse stretcher leaves TOD uncompensated, the propagation power and distance within the SMF should be carefully selected so that the gain from the nonlinear pulse spectral broadening is not overwhelmed by the adverse effects from the unbalanced TOD. In our current endomicroscope system, we chose a 30-cm-long SMF to better accommodate the commonly use range of P_{DCF} (i.e., ~15 − 45 mW) at varying center wavelengths (thus varying P_{SMF}/P_{DCF} ratios).
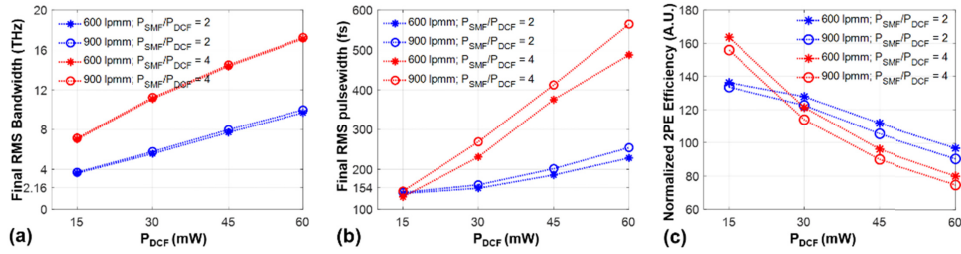
Fig. 5. The influence of grating density on the final dispersion compensation efficacy for the grating pair-based spectro-temporal dispersion management scheme. With SMF length fixed at 40 cm, the final rms bandwidth (a), rms pulsewidth (b), and normalized 2PE efficiency (c) at different power configurations are compared between the 600-lpmm and 900-lpmm grating pairs. The rms bandwidth and rms pulsewidth for the initial transform-limited pulse (890-nm center wavelength, 80-MHz repetition rate), ~2.16 THz and ~154 fs, are indicated in subfigures (a) and (b) respectively.

4.2 Dependence on the groove density of grating

We then investigated the influence of grating density on the compensation efficacy. An example comparison with L_{SMF} fixed at 40 cm is illustrated in Fig. 5. First, for a given P_{SMF}/P_{DCF} ratio, the grating density has negligible influence on the final spectral bandwidth (Fig. 5a). This suggests that the final spectral bandwidth is mainly decided by the interplay between SPM and GVD during propagation, since the negative GDD provided by the 600- and 900-lpmm grating pairs are the same for given SMF and DCF length. Secondly, the 600-lpmm grating (asterisk-marker curves) outperforms the 900-lpmm grating (circle-marker curves) at all P_{DCF} (for both $P_{SMF}/P_{DCF} = 2$ and $P_{SMF}/P_{DCF} = 4$) in both rms pulsewidth (Fig. 5b) and the normalized 2PE efficiency (Fig. 5c, by ~5-10% in general). Similar results were also observed for other SMF lengths (data not shown for brevity).

Given a grating pair, denoting the groove period by d and the incident and diffraction angles by θ_i and θ_d, respectively, the ratio between TOD and GDD generated by the grating pair can be found from Eqs. (5-6) as

$$\frac{\text{TOD}}{\text{GDD}}(\omega,d) = -\frac{3}{\omega} \cdot \left(1 + \frac{\lambda}{d} \cdot \frac{\sin\theta_d}{\cos^2\theta_d}\right) \overset{\text{L.C.}}{=} -\frac{3}{\omega} \cdot \frac{1 + \left(\frac{\lambda}{2d}\right)^2}{1 - \left(\frac{\lambda}{2d}\right)^2} , \tag{14}$$

where the last step assumes the Littrow configuration (L.C.), i.e., $\sin\theta_i = \sin\theta_d = \lambda/(2d)$, adopted in both simulation and experiment. From Eq. (14), one can easily tell that a denser grating with smaller line period d yields a larger TOD-to-GDD ratio, thus adding more TOD to the pulse and impairing the overall efficacy of dispersion compensation, as observed in our simulation study. Therefore, gratings of lower groove densities are preferable for the sake of performance; but given that the GDD compensation power of a grating pair scales quadratically with its density (see Eq. (6)), a good trade-off between the compensation efficacy and the inter-grating separation (i.e., the footprint of the setup) should be considered, especially when working with long endomicroscopes and shorter excitation wavelengths (that are associated with a higher GDD in optical fibers).
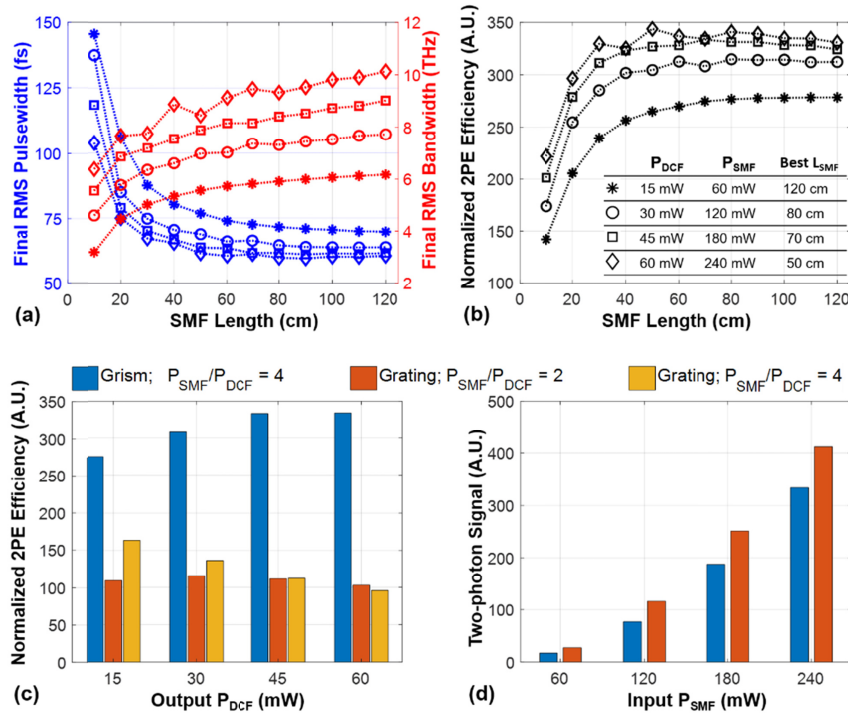
4.3 Comparison with an ideal grism-pair stretcher

Fig. 6. Efficacy comparison between the grism- and grating-based spectro-temporal dispersion compensation schemes. The dependence of final rms bandwidth and pulsewidth (a), and normalized 2PE efficiency (b) on varying SMF lengths and DCF powers are plotted with the SMF-to-DCF power ratio fixed to 4 (which corresponds to the best practical scenario). Different DCF powers are represented by different marker types, and the best SMF length for each power configuration is listed in the legend. (c) Comparison of the normalized 2PE efficiency between the grism- and grating-based compensation methods at various DCF powers and SMF-to-DCF power ratios. (d) Comparison of the final absolute two-photon signal strength between the grism- and grating-based compensation methods at various input SMF powers. Here the grating density is fixed to 600 lpmm, and the center wavelength is 890 nm.

In light of the detrimental effects of the uncompensated TOD, a grism-pair pulse stretcher which is capable of providing independently tunable anomalous GDD and TOD [25] has become a preferable choice for dual-fiber-based spectro-temporal dispersion compensation, and a final pulsewidth down to ~30 fs FWHM has been reported [26–28]. One major limitation of the grism pair, however, is the poor power efficiency. As the laser beam needs to go through grating diffraction for 4 times and air-glass refraction on prism surfaces for 16 times, the best overall throughput hitherto reported (even with antireflection coating) is ~30% [25,27,28]. Considering a typical fiber-coupling efficiency of ~80%, the propagation power in DCF is at most 25% as high as that in the SMF; therefore, the SMF-to-DCF power ratio is set to 4 for a grism-based stretcher in our simulation.

First, with TOD also compensated, the evolution of pulsewidth with SMF length scales well with the reciprocal of corresponding spectral bandwidth as evident in Fig. 6a. Secondly, the final 2PE efficiency benefits from both a longer propagation distance and a higher SMF power (Fig. 6b). Moreover, for all power levels studied here, the final 2PE efficiency first increases rapidly with longer propagation distance in the SMF (up to ~40 cm), then gradually saturates and stays generally stable (with only a slight decreasing trend after the SMF length exceeds the respective optimal values). This is in distinct contrast to what we have observed in the grating-pair case (Fig. 4c), where the final 2PE efficiency drops quickly after the SMF

length exceeds the optimal length. Since both longer propagation and higher SPM power promote SPM-induced spectral broadening, the observation reflects the robustness of a grism pair against TOD accumulation from extra propagation in the SMF.

To investigate the extent to which an ideal grism-based pulse stretcher can further enhance the compensation efficacy, we should compare the respective optimal scenarios from the grating pair and grism pair cases. For the grism-pair case, we choose L_{SMF} = 80 cm with the SMF-to-DCF power ratio set to 4. For the grating-pair compensation scheme (600 lpmm chosen for better performance), we choose L_{SMF} = 20 cm over other SMF lengths since it yields overall higher normalized 2PE efficiencies when taking into account all power configurations (see Fig. 4c). With these choices, the best normalized 2PE efficiency obtained with a grating-pair stretcher is compared with that obtained with an ideal grism pair at varying P_{DCF} levels (Fig. 6c). Clearly the grism pair affords ~2- to ~3-fold improvement on the normalized 2PE efficiency; and as expected, the extent of signal enhancement becomes more profound at higher P_{DCF} (also higher P_{SMF}) values.

On the other hand, we are also concerned with the maximal absolute two-photon signal obtainable with a given input power P_{SMF}. To check this parameter, we pick the high throughput cases (i.e., P_{SMF}/P_{DCF} = 2) for the grating-pair approach and calculate the absolute two-photon signal strength as defined in Eq. (12). As shown in Fig. 6d, this time the ~2-fold higher power throughput afforded by a grating pair can outbalance its deficit in the normalized 2PE efficiency (i.e., the pulse profile) and result in an overall stronger two-photon signal than the grism counterpart with the same given input power to the SMF.

Furthermore, it is worth noticing that achieving the optimal grism throughput of ~30% at the design wavelength requires: 1) anti-reflection coating on the prism surfaces, and 2) meticulous selection or even customization of the apex angle of the prism and the blaze angle of the reflective gratings so that the incident angle on the grating as prescribed by the target anomalous GDD-to-TOD ratio lies close to the grating's blaze angle (also the Littrow angle). As the target GDD-to-TOD ratio is wavelength-dependent, the beam path through the grism pair also needs to be adjusted accordingly (typically by rotating the entire grism-pair setup) to accommodate the varying wavelength. Therefore, at non-optimal wavelengths the incident angles on both grating and prism surfaces deviate from the respective design values, and as a result the overall throughput could drop quickly (down to <10% based on our experience). Given that the safe laser power allowed in a typical SMF is limited to ~500 mW, a severe power loss in the grism setup limits the obtainable excitation power from the endomicroscope and thus the imaging depth in biological tissues and imaging quality.

To summarize, for bench-side scenarios with an abundant input power (e.g., from a Ti:Sapphire laser), a grism pair generally yields a stronger two-photon signal with a given P_{DCF}, as long as its throughput is specially optimized for the excitation wavelength. When the input power budget is limited, e.g., when building a portable endomicroscopy system using a compact fiber laser, the grating pair could be a better choice in terms of both signal expectation and setup simplicity. We would like to point out that, although the grating pair's two-photon signal advantage with a given input laser power involves a much higher laser power incident on the specimen, it still possesses significant practical value. For example, in the context of deep-tissue two-photon imaging, a higher laser power on the tissue surface is necessary for overcoming scattering loss so that sufficient ballistic photons can reach the target deep focus, with the laser intensity (power per area) still staying safe everywhere.

5. Discussions

Another alternative for dispersion compensation is to use a prism pair, which provides GDD and TOD of the same sign and therefore counteracts rather than increases the existing TOD in optical fibers. However, the compensation capability afforded by a prism pair is generally much lower; even with highly dispersive prisms, a prohibitive inter-prism separation on the

order of meters is needed to provide adequate anomalous GDD for an only 1-meter-long silica fiber [15]. Therefore, the prism pair is poorly applicable for a practical fiber-optic two-photon endomicroscope.

Our simulation study suggests that, compared with a grating pair, the grism-pair stretcher can indeed further improve the efficacy of spectro-temporal dispersion compensation and enhance the 2PE efficiency. In the context of practical fiber-optic two-photon endomicroscopy imaging, however, the signal enhancement obtainable by switching from grating to grism can fall below the expectation from simulation. One practical challenge is associated with the significantly broadened spectral bandwidth of the final ultrafast laser pulses. Fundamentally, the SPM-induced spectral recompression in the DCF, where the propagation power is much lower, cannot fully revert the preceding spectral broadening in the SMF. According to simulation, the root-mean-square (RMS) spectral bandwidth [18] can be easily expanded by 4- to 5-fold (data not shown), which also matches previous reports of sub-30-fs pulsewidth obtained from an initial 150-fs FWHM pulsewidth [27,28]. Moreover, the actual wavelength span (not in the RMS sense) of the final pulse can approach ~100 nm wide (red-colored curve in Fig. 2a). To tightly focus such a broadband laser beam with high NA (at least ~0.6) imposes demanding requirements on the miniature objective design. Considering the notable spherical and chromatic aberrations of standard graded-index (GRIN) lenses [29,30], a more sophisticated high-performance miniature objective of minimal aberration and excellent achromaticity is needed to realize the 2PE advantage promised by the grism pair [31–33].

Overall, we believe that a grating pair-based pulse stretcher features unique merits for the dual-fiber spectro-temporal dispersion compensation scheme in a fiber-optic two-photon endomicroscopy system. Compared with the prism pair, it features much effective GDD compensation and thus a more compact footprint. Compared with a grism pair, it affords a higher power throughput and superior wavelength versality, i.e., one setup can well accommodate a broad wavelength range (at least from 730 to 920 nm in our experience). Moreover, the grating pair's advantage in power throughput can potentially make up for its shortage of uncompensated TOD, therefore finding its unique niche in two-photon endomicroscopic systems and biomedical imaging applications with limited input power budget.

Fundamentally, given any target pulse profile (amplitude and phase) out of the DCF, the desired input pulse profile can be calculated via reversely propagating the target output pulse backwards through DCF (i.e., time reversal). Then an ideal pulse shaper can be built to generate this desired input pulse profile, typically based on raw pulses from some laser source [34]. In the dual-fiber spectro-temporal dispersion compensation scheme, the nonlinear propagation in the first fiber (i.e., the SMF) and the following negative chirping in the grating pair work in concert as a pulse shaper. With negative chirping properly tuned, the original transform-limited pulse profile from the Ti:Sapphire laser is shaped into a best approximation of the desired input pulse profile for the DCF. Due to the unbalanced higher-order dispersion and unmatched propagation power in the SMF and in the DCF, such a pulse shaper is suboptimal. Other pulse shaper implementations that lend themselves to a more efficient fiber delivery of femtosecond laser pulses deserve future investigation [35].

6. Conclusions

In summary, we have undertaken a comprehensive analyses and characterization of the dual-fiber spectro-temporal dispersion compensation scheme with a grating pair serving as the pulse stretcher in the context of fiber-optic two-photon endomicroscopy imaging. The dispersion compensation efficacy of this setup was experimentally confirmed as enhancing the two-photon signal by ~3-fold compared with the linear-only single-fiber counterpart. Furthermore, with the aid of numerical simulation, we have also examined the influence of several key design parameters (including the length of SMF, the propagation powers in both

fibers, and the grating density) on the overall dispersion compensation efficacy and proposed several design and operational guidelines such as using a shorter SMF and lower-density gratings if possible. We have also evaluated the extent of two-photon signal enhancement promised by cancelling the TOD and GDD simultaneously with an ideal grism-pair pulse stretcher. The comparison study reveals that although in general the grism-pair stretcher can substantially enhance the overall 2PE efficiency, the grating-pair stretcher features much higher power throughput, which can outbalance its deficit in compensation efficacy and thus generate more nonlinear signal photons per input SMF laser power. Such advantage in input power economy, along with its engineering simplicity and remarkable wavelength versality, makes the grating pair the preferable pulse stretcher choice for applications with a limited power budget, for example, when building a portable endomicroscopy system powered by a compact femtosecond fiber laser [36,37].